A Mixed-Signal Control System for Lorentz-Force Resonant MEMS Magnetometers

Josep Maria Sánchez-Chiva, Juan Valle, Daniel Fernández, and Jordi Madrenas

***Abstract*— This paper presents a mixed-signal closed-loop control system for Lorentz force resonant MEMS magnetometers. The control system contributes to 1) the automatic phase control of the loop, that allows start-up and keeps self-sustained oscillation at the MEMS resonance frequency, and 2) output offset reduction due to electrostatic driving by selectively disabling it. The proposed solution proof-of-concept has been tested with a Lorentz force-based MEMS magnetometer. The readout electronic circuitry has been implemented on a printed circuit board with off-the-shelf components. Digital control has been implemented in an FPGA coded with VHDL. When biased with 1 V and a driving current of 300 μA_{rms}, the device shows 9.75 pA/μT sensitivity and total sensor white noise of 550 nT/$\sqrt{\mathrm{Hz}}$. Offset when electrostatic driving is disabled is 793 μT, which means a 40.1% reduction compared when electrostatic driving is enabled. Moreover, removing electrostatic driving does not worsen bias instability, which is lower than 125 nT in both driving cases.**

***Index Terms*— MEMS, magnetic sensor, magnetometer, Lorentz force, offset suppression, digital control.**

I. Introduction

IN THE last years, the rise of smartphone market and other hand-held devices have made researchers to focus their efforts in the design of low-cost, low-power and low-area inertial sensors. Accelerometers and gyroscopes are examples of these research outcomes as they were the first sensors based on MEMS technology massively introduced in the market [1], [2]. In contrast, to the best of our knowledge, it still does not exist a commercial MEMS-based magnetometer even though Lorentz force based MEMS magnetometers were first proposed in the late 90's [3], [4]. Current commercial magnetometers in high volume applications are mostly Hall sensors [5], Anisotropic Magnetoresistors (AMR) [6], Tunnel Magnetoresistors (TMR) [7] and Giant Magnetoresistors (GMR) [8]. However, their main disadvantages is the need of materials not compatible with standard manufacturing processes and their high current consumptions [9], [10].

Manuscript received March 11, 2019; revised April 15, 2019; accepted April 15, 2019. Date of publication April 29, 2019; date of current version August 6, 2019. This work was supported in part by the Spanish Ministry of Science and Innovation and in part by the European Social Fund (ESF) under Project TEC2015-67278-R. The work of J. M. Sánchez-Chiva was supported by the Secretaria d'Universitats i Recerca del Departament d'Empresa i Coneixement de la Generalitat de Catalunya and in part by ESF. The associate editor coordinating the review of this paper and approving it for publication was Prof. Boby George. *(Corresponding author: Josep Maria Sánchez-Chiva.)*

J. M. Sánchez-Chiva, J. Valle, and J. Madrenas are with the Department of Electronic Engineering, Universitat Politècnica de Catalunya, 08034 Barcelona, Spain (e-mail: jose.maria.sanchez.chiva@upc.edu; juan.valle.fraga@upc.edu; jordi.madrenas@upc.edu).

D. Fernández is with Nanusens, 08290 Cerdanyola del Vallès, Spain (e-mail: daniel.fernandez@nanusens.com).

Digital Object Identifier 10.1109/JSEN.2019.2913459

Given their good sensitivity and low power consumption, Lorentz force based MEMS magnetometers have become a hot topic with numerous publications in the last years [11]–[23]. Moreover, taking advantage of the Back-End-Of-Line (BEOL) metal layers in a CMOS technology [24], it is possible to integrate Lorentz force magnetometers together with accelerometers and gyroscopes in the same die area of the electronics [25], [26], thus, reducing fabrication cost and area.

Current advances in the literature of MEMS magnetometers can be divided into two groups. On one hand, new MEMS devices in different technologies have been proposed [11]–[14]. On the other hand, in order to generate the Lorentz force, AC current driving is needed, which upconverts the measured baseband magnetic field into a double-sideband signal around the driving current frequency. Then, an electrostatic drive may be applied, whose phase respect to current driving can make the output signal to be amplitude [15] or frequency modulated [11]. For this reason, new modulation techniques are an important part of the literature. Also, the technique used to drive the sensor, either using open- or closed-loop has received researchers interest [11], [12], [16]–[23]. This work is focused in two important aspects to take into account if MEMS magnetometers are to be introduced in the market. First, phase locking of the closed-loop to get self-sustained oscillation at the device resonance frequency, and second, offset minimization.

A. Phase Locking

Given that the modulation is normally done at the mechanical resonance frequency, and that it changes with temperature, it is of utmost importance to track it in order to get maximum and constant gain. To do so, various strategies have been found in the literature. In [15] and [27] digital lock-in amplifiers are used to close the loop. This solution has been used as a proof-of-concept of the modulation strategies proposed, but it requires bulky commercial devices. In [20] an off-chip resonator has been used to track the resonance frequency, but it does not provide this tracking with temperature variations. Similarly, in [21] an on-chip resonator was especially designed for this purpose. Even though it proved to track the resonance frequency with temperature variations, it requires extra design effort and the use of important chip area. Another approach is to set the MEMS magnetometer in a self-sustained oscillation by placing it in a closed loop with an overall 0° phase. In this case, the MEMS resonator works as an LC tank, setting the loop oscillation frequency to its resonance frequency.

1558-1748 © 2019 IEEE. Translations and content mining are permitted for academic research only. Personal use is also permitted, but republication/redistribution requires IEEE permission. See http://www.ieee.org/publications_standards/publications/rights/index.html for more information.

This strategy is used in [11] and [12] with low phase-noise and good frequency stability. However, manual phase adjustments are required, which are not acceptable for high-volume applications.

In this work, a robust self sustained oscillation loop implemented in the digital domain is proposed. This adds flexibility to the signal processing and provides a low power consumption compared with analog strategies given that digital circuits may be driven with a lower supply voltage. Moreover, phase adjustment has been implemented, which allows to automatically tune the phase for each device, making it Process-Voltage-Temperature variation tolerant.

B. Offset Minimization

When magnetic field is amplitude modulated (AM), electrostatic driving feedthrough introduces an important amount of offset that must be removed [15], [27]. In order to avoid this offset, some works do not drive the MEMS electrostatically and track frequency with on- and off-chip oscillators [20], [21], but requiring extra area consumption and design time. In [15], current chopping is proposed to get rid of this offset, but magnetic field requires an extra modulation step, which increases power consumption. Given that electrostatic driving is not necessary to perform an AM, it may be disabled when the output signal is large enough to sustain oscillation. For example, when the sensor suffers hard iron effects or when it is measuring large magnetic fields. Then, when this signal is low, such as when measuring small magnetic fields, it could be enabled again.

In this work, an electrostatic driving control system is proposed, enabling it when sensor output is dangerously low to sustain oscillation, and disabling it when hard-iron effects are present or large magnetic fields are measured. Doing so, offset can be greatly minimized in some cases and the range of maximum measurable field is increased.

II. MEMS Sensor Working Principle

The MEMS magnetometer uses the Lorentz force to detect magnetic fields. This force principle states that a moving charged particle suffers a force under the presence of a magnetic field. In the case of MEMS magnetometers, those moving charged particles are the current electrons flowing through the MEMS structure. Given that a current $\vec{I}$ flows through a structure of length L, the resulting Lorentz force ($\vec{F_L}$) is

$$\vec{F_L} = L\vec{I} \times \vec{B} \tag{1}$$

where $\vec{B}$ is the magnetic field being measured. When electrostatically driven, the sensor response can be described with the second order mass-spring-damper function

$$m\ddot{z} + b\dot{z} + kz = F_E + F_L \tag{2}$$

where, for our device, $m \approx 0.2\ \mu g$ is the device rotor mass, $b \approx 1.5 \cdot 10^{-6}\ Ns/m$ is the damping coefficient, and $k \approx 175\ N/m$ is the spring constant. These parameter have been derived from wafer level measurements. $F_E \approx V \cdot \upsilon \cdot C_s/g$ is the electrostatic driving force that is a function of the device DC voltage V, the electrostatic driving υ, the sensor capacitance C_s and its gap g. Finally, F_L is the resulting Lorentz force when a magnetic field orthogonal to the current direction is applied to the device. More details about the MEMS parameters are given in section III. In the case of an amplitude modulated magnetometer, the electrostatic and current driving are in phase, and so are F_E and F_L. The electromechanical model of the device is shown in Fig. 1. When the MEMS is subject to harmonic excitations at the device resonance frequency $f_r = \omega_r/2\pi$, the vibration amplitude A_z can be derived from (2).

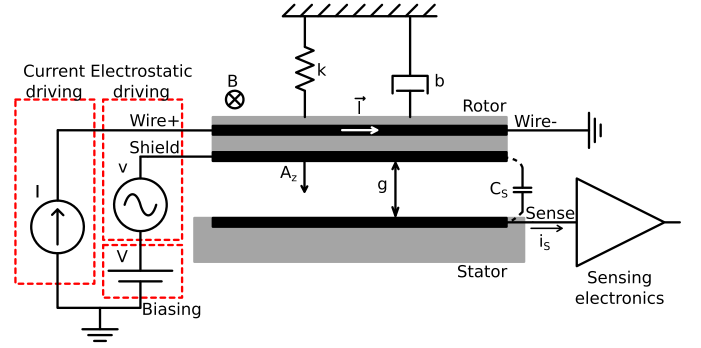

Fig. 1. Simplified MEMS and readout electronics diagram with the device electromechanical model.

$$A_z(f_r) = \frac{Q}{k}(F_L + F_E) \approx \frac{Q}{k}\left(I \cdot L \cdot B + V\upsilon\frac{C_s}{g}\right) \tag{3}$$

where $Q = \sqrt{k\,m}/b$ is the device quality factor. Then, the capacitance variation ΔC_s due to the displacement in (3) can be obtained.

$$\Delta C_s = \frac{\epsilon_r\epsilon_0 A}{g} - \frac{\epsilon_r\epsilon_0 A}{g + \frac{Q}{k}\left(I \cdot L \cdot B + V\upsilon\frac{C_s}{g}\right)} \tag{4}$$

where A is the device equivalent capacitor area, ϵ_r is the air relative permittivity, and ϵ_0 is the absolute permittivity. When the MEMS sensor has a non zero DC voltage, the variation of the device capacitance due to both the current I and electrostatic υ drivings generates a current $i_s = dq(t)/dt$ in (5) as a consequence of charge movement that is sensed by the readout electronics connected to the stator electrode as depicted in Fig. 1.

$$i_s \approx \frac{\epsilon_r\epsilon_0 A Q}{g^2 k} V\omega_r\left(\underbrace{I \cdot L \cdot B}_{\text{signal}} + \underbrace{V\upsilon\frac{C_s}{g}}_{\text{offset}}\right) \tag{5}$$

whose sensitivity to magnetic field is

$$S = \frac{\partial i_s}{\partial B} = \frac{V\omega_r\epsilon_r\epsilon_0 A L Q}{g^2 k} I_{rms} \tag{6}$$

that is proportional to driving current and DC voltage, parameters that can be tuned on the manufactured MEMS.

III. Device Description

The Lorentz-force magnetometer used in this study was built using the BEOL metal and oxide layers of a 6-Metal 0.18 μm

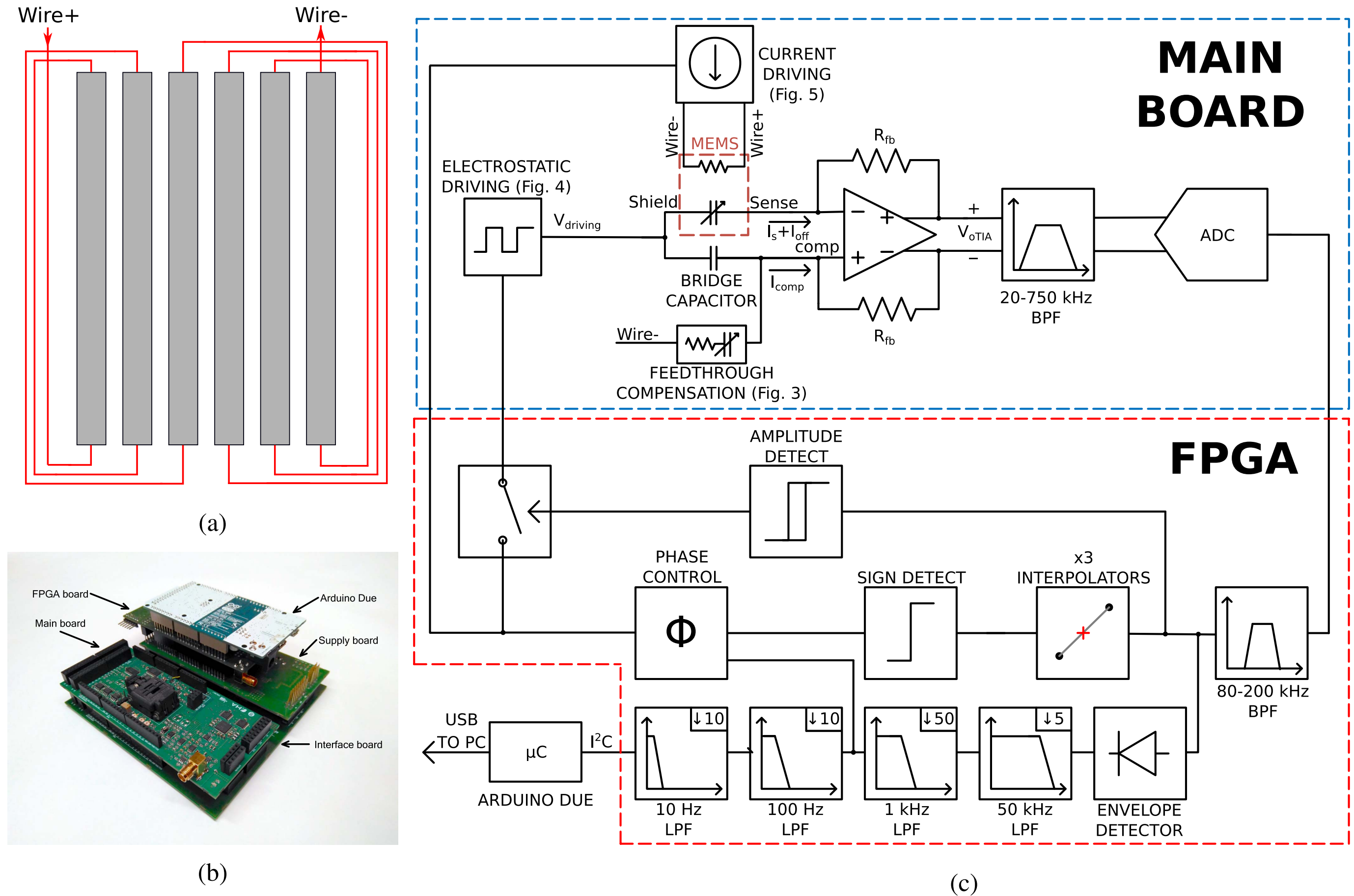

Fig. 2. MEMS magnetometer Wire structure sketch in (a), stack of designed PCBs in (b) and system block-level schematic in (c).

CMOS-MEMS process [28], [29]. Vapor hydrofluoric (vHF) acid, which provides both good metal to silicon oxide selectivity [30] and uniformity [29], was used to release the MEMS structures by etching the sacrificial oxide at wafer-level. The passivation layer was modified by the foundry to be vHF resistant by increasing its silicon content [29], [31]. It was then used as a masking layer during the release process, protecting the regions that were not to be etched. Passivation windows were open in the MEMS areas to allow vHF penetration and subsequent sacrificial oxide removal. After the release, the devices were vacuum sealed at $1-10\ mbar$ approximately using a thin Aluminium sputtered layer that covered the MEMS magnetometers. Finally, the wafers were diced and the devices wire-bonded in QFN packages.

Many Lorentz-force magnetometers have a single current-carrying wire. However, the Lorentz-force magnetometer tested in this study is formed by 20 parallel current-carrying wires, so the current needed to achieve a given sensitivity is significantly reduced. A simplified diagram of the current-carrying wires is depicted in Fig. 2a. Firstly, ten clamped-clamped cantilevers are mechanically coupled so they resonate at a single frequency. Secondly, two parallel current-carrying wires run along each cantilever. In addition, in order to further improve sensitivity, the clamped cantilevers are designed as long as possible (600 μm), without jeopardizing their mechanical reliability. This allows to both minimize the system stiffness and to maximize the Lorentz-force, linearly dependent on cantilever length. The sensing electrodes are disposed on the side of the clamped-clamped cantilevers, so the capacitance changes only when there is lateral movement in first approximation. Lateral displacement is only caused by an out-of-plane magnetic field, which is perpendicular to the Lorentz current. Therefore, the tested magnetometer is single-axis as it detects magnetic field only in the out-of-plane direction.

The sensing gap between rotor and stator is $g = 0.5\ \mu m$ and the total sensing area is around $A \approx 30000\ \mu m^2$. The approximate system stiffness is $k \approx 175\ N/m$, referred to an uniform load and the displacement at the central part of the cantilever. The resonating bridges were made of a combination of oxide and metal layers 2, 3, 4, and 5.

Finally, it is important to note that the current-carrying Lorentz wires were completely surrounded by a single metal electrode which acts as an electrical shield and as the external part of the clamped-clamped cantilever. This way, the changing electrical potential of the Lorentz wires can be isolated from the sensing electrodes, greatly simplifying interference filtering. In the electronic domain, depicted in Fig. 2c, it means that Wire and Sense nodes parasitic capacitance is virtually 0 fF, even though it was measured to be 30 fF after packaging.

As depicted in Fig. 2c, the sensing electrode connected to the driving circuitry has been named Shield because it is also connected to the shielding structure of the current carrying wires. Sensing electrode connected to the amplifier is referenced as Sense. Finally, the electrodes giving off-chip access to the sensor current carrying wires will be named Wire+ and Wire-.

IV. Sensing Electronics

The proposed system block diagram is shown in Fig. 2c. A series of printed circuit boards (PCB) has been designed in order to implement a modular system and perform the measurements. The boards have been designed with the same form factor of the microcontroller board that provides connectivity with the host computer: Arduino Due [32]. The stack of boards is shown in Fig. 2b and it consists of: 1) Arduino Due, that communicates with the FPGA using I^2C protocol, 2) Supply board, that contains DC-DC converters and linear regulators to generate the needed voltage rails, 3) FPGA, used to read the ADC, control the DACs that generate the electrostatic and current drivings and the loop necessary digital blocks, 4) the main board, where the MEMS under test has been placed within a clamp-type socket, as well as the readout circuit, and 5) an interface board, that is used to separate the Arduino and FPGA boards from the sensor in order to minimize digital noise.

A. Half Bridge

In order to allow single-ended to differential conversion of the sensor signal, as well as reducing feedthrough from the electrostatic driving, a half Wheatstone bridge has been used. This bridge capacitance has been implemented with precision capacitor trimmers. Even though the sensor was designed and packaged to have a very low Wire to Sense parasitic capacitance, socket and PCB routing are expected to create some parasitics. For this reason, a capacitive network has also been designed and implemented in order to reduce feedthrough due to the current driving. Both compensation nets have been connected as the sensor differential capacitance, as depicted in Fig. 2c and further detailed in Fig. 3. Adjusting capacitance C_{W-C} allows to compensate the feedthrough due to the current driving. It is worth to mention that CMOS-MEMS integrated designs having the sensor and the readout electronics in the same die area may make this trimming unnecessary: Wire to Sense parasitic capacitance may be importantly reduced by having shorter and shielded nodes.

B. Amplification and Filtering

A Transimpedance Amplifier (TIA) has been used to sense and amplify the sensor output current

$$\begin{aligned} V_{o\ TIA}(t) &= R_{fb}(i_s + i_{off} - i_{comp}) \\ &= R_{fb}(S \cdot B + i_{off} - i_{comp}) \end{aligned} \quad (7)$$

where R_{fb} is the TIA feedback resistance, i_s is the sensor current in (5), i_{off} is the offset due to current driving feedthrough depicted in Fig. 2c, and i_{comp} is the current from the bridge

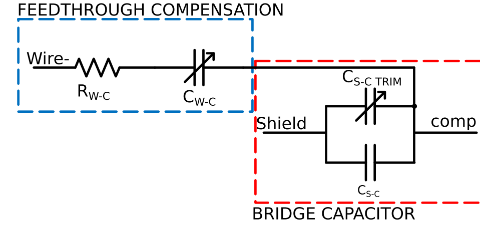

Fig. 3. Wire to Sense parasitic capacitance compensation net (blue box) connected between Wire- and the comp node (“Feedthrough compensation” block in Fig. 2). Wheatstone half-bridge compensation capacitance (red box) connected between Shield node, where $V_{driving}$ is injected, and comp node, the Sense complementary node in the differential branch (“Bridge capacitor” block in Fig. 2c).

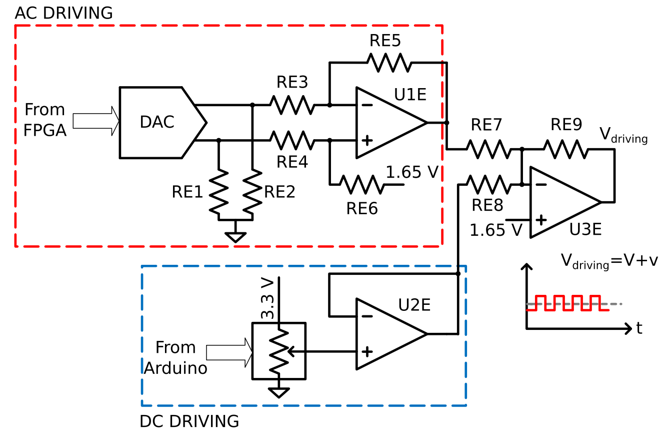

Fig. 4. Electrostatic driving schematic (“Electrostatic driving” block in Fig. 2c).

capacitor and the current feedthrough compensation network in Fig. 3. The expression is also shown as a function of sensitivity S in (6) and the magnetic field B. Next, the signal is filtered using a bandpass filter with 20 dB gain. Finally, an ADC working at 5.55 MHz sampling frequency digitizes the signal and sends it to the FPGA.

C. Electrostatic and Current Driving

Sense node voltage is set by the TIA common-mode voltage at mid-supply and Shield voltage is set by a digital potentiometer. A DAC has been used to generate the AC part of the electrostatic driving. AC driving has been designed to be much lower than DC driving in order to make the MEMS device to work in the linear region. Both AC and DC voltages are then added with an opamp and driven to the sensor Shield node, as shown in Fig. 4. An improved Howland floating current source driven by a high speed DAC has been implemented to perform the MEMS current driving, allowing a maximum output current of 5 mA_{rms} [33]. It has been implemented with floating load in order to minimize supply rails noise, and to control the center DC voltage of the signal [17].

V. Noise Analysis

Implementing the electronics with off-the-shelf components does not allow the best performance due to the various parasitics that appear in the sensor connection with the TIA.

From all the components that introduce noise to the system, the following have been considered: the TIA, the Howland current source and the ADC quantization noise as well as the MEMS sensor Brownian noise. Given that the sensor resonates well beyond the noise corner frequency, only white noise has been considered in the analysis.

A. Sensor Thermomechanical Noise

Spectral noise density equivalent force for MEMS sensors was described in [34], where MEMS noise is associated with its damping coefficient b. In order to obtain an equivalent output noise current for a force noise, first, sensitivity to a force has been obtained by deriving (5) as a function of force

$$S_F = \frac{\partial i_s}{\partial F} = \frac{\epsilon_r \epsilon_0 A Q V \omega_r}{g^2 k} \tag{8}$$

Then, (8) is multiplied by the noise force

$$\overline{i_s} = \frac{\epsilon_r \epsilon_0 A Q V \omega_r}{g^2 k}\sqrt{4 k_B T b} \approx 1.33\ pA/\sqrt{Hz} \tag{9}$$

where k_B is the Boltzmann constant, $T = 300\ K$ the device temperature, sensing area $A \approx 30000\ \mu m^2$, gap $g = 0.5\ \mu m$, spring constant $k \approx 175\ N/m$, damping coefficient $b \approx 1.5 \cdot 10^{-6}\ Ns/m$, quality factor $Q = 1500$, resonance frequency $f_r = 146\ kHz$, and $V = 1\ V$.

B. Amplifier Noise

The opamp used to implement the TIA is the low noise, low bias current Texas Instruments THS4121 [35]. Only opamp input-referred noise and feedback resistors' noise have been considered. First, from its equivalent input voltage noise $\overline{v_{OA}}$, the equivalent current noise referred to the sensor is

$$\overline{i_{s\ OA}} = \sqrt{2}\,\overline{v_{OA}}\,\omega_r (C_s + C_p + C_{U-W-C}) \tag{10}$$

where C_p is the parasitic capacitance between Sense node and ground, C_{U-W-C} is the resulting parasitic capacitance between Wire and Sense after compensation by circuit in Fig. 3, and C_s is the sensor capacitance. Note that the $\sqrt{2}$ factor corresponds to the translation of the differential noise into a single ended noise referred to the MEMS. In this work, C_p is expected to be in the order of tens of pF [21] due to the chip pad, packaging, through-hole socket pin, PCB routing and the opamp input capacitance. Considering a rough estimate of $C_p = 50\ pF$ results in a noise of $\overline{i_{s\ OA}} = 0.368\ pA/\sqrt{Hz}$. Moreover, this is a high impedance node, so even tough PCB tracks have been shielded and accurately routed, through hole socket pads and wire bonding are still prone to noise pick up.

The second important noise source in the TIA are feedback resistors $R_{fb} = 1\ M\Omega$ noise (11).

$$\overline{i_{s\ R_{fb}}} = 2\sqrt{\frac{4 k_B T}{R_{fb}}} = 0.257\ pA/\sqrt{Hz} \tag{11}$$

C. Howland Current Source Noise

Howland current source resistors have been set to low values in order to match resistors and opamp noise [36]. Doing so, the dominating noise sources of the circuit in Fig. 5, which are $U1_H$, $U3_H$ opamps and R_{H3}, R_{H4}, R_{H5}, R_{H6} resistors

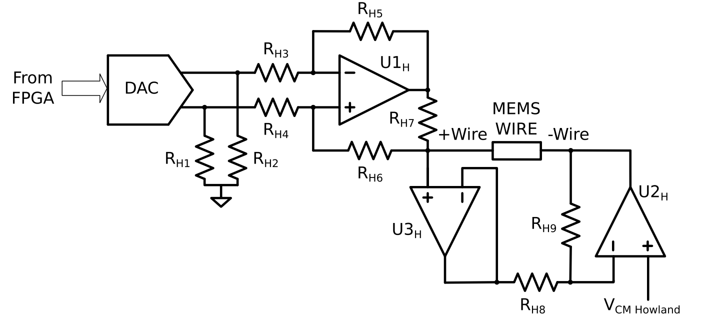

Fig. 5. Current-driving block for the MEMS Wire, based on an improved floating Howland current source [33] ("Current driving" block in Fig. 2c).

are below 70 $pA/\sqrt{Hz}$ at the output of the Howland circuit. As a consequence, total output current noise of the improved Howland current source is $\overline{i_H} = 163.1\ pA/\sqrt{Hz}$. This current noise is translated in two ways to the sensor output current. First, it is converted to sensor output current noise by means of Lorentz force as described in (5), which results in a negligible noise. Second, this noise is coupled to the sensor output current through the parasitic capacitance between Wire and Sense nodes which results in a noise feedthrough directly to the Sense node. Even though the exact value of this capacitance is unknown, a rough estimate of $C_{U-W-C} < 2\ pF$, together with MEMS current carrying wires resistance of around $R_{Wire} = 3\ k\Omega$, results in an output noise of

$$\overline{i_{s\ Hpar}} = \overline{i_H} R_{Wire} 2\pi f C_{U-W-C} < 0.90\ pA/\sqrt{Hz} \tag{12}$$

D. Quantization Noise

Quantization rms noise due to the analog to digital conversion [37] can be expressed as sensor equivalent output noise by dividing it by the gain stages of the amplification chain. In this case, gain is a transimpedance $Z_C = 10\ M\Omega$ which accounts for the TIA transimpedance and the filters gain.

$$\overline{i_{s\ q}} = \frac{\sqrt{2} V_{LSB}}{\sqrt{12}\ Z_C\ \sqrt{BW}} = 1.33\ fA/\sqrt{Hz} \tag{13}$$

where $V_{LSB} = 54.3\ \mu V$ is the voltage of one LSB and $BW = 2.775\ MHz$ is the ADC bandwidth.

E. Total Expected Noise

With the noise figures obtained for each sub-circuit, and the measured sensor sensitivity, total noise is expected to be around 171 $nT/\sqrt{Hz}$. It must be taken into account, though, that various approximations have been done during the process, such as Wire to Sense, and Sense parasitic capacitances which have been described throughout the section.

VI. Digital Implementation

The block diagram of the digital part has been included in Fig. 2c. Once the signal is in the digital domain, it is filtered again with a 120 kHz bandwidth finite-impulse response (FIR) band-pass filter. Doing it in the digital domain allows the use of more selective filters. Then, the signal follows two paths: the path to demodulation and the path to close the loop. In the

first one, the signal is demodulated with an envelope detector followed by four FIR low-pass filters of 50 *kHz*, 1 *kHz*, 100 *Hz* and 10 *Hz*. The purpose of applying four filters is twofold. First, by decimating the signal, the filters can be designed to have a lower set of coefficients, being more area efficient. Second, the 1 *kHz* filter output is used by the phase control block, while the 10 *Hz* filter output is stored in the registers of an I^2C slave block before being sent to the processor.

In the second path, i.e. the path to close the loop, the signal is used to generate a clock at the same frequency that is injected back into the device to achieve phase locking in the loop and sustain oscillation. After the bandpass filter, the signal is interpolated with three cascaded linear interpolators. These interpolators have two objectives. First, given that during zero crossing, signal is expected to have the highest slope, each interpolator improves the resolution of the zero-crossing detector by a factor of two, improving time resolution of zero-crossing detector from 180 *ns* (sampling period) to 22.5 *ns* when assuming a linear signal. Second, increasing the number of samples per period also increases the resolution of the phase adjustment by reducing the minimum phase step.

Next, a zero-crossing detector is implemented by taking the sign bit of the two's complement signal. Zero-crossings of the signals are used to generate a square signal that tracks the MEMS resonance frequency. This square signal is introduced to the phase control block, a 1024-bit shift register that is used to adjust the signal phase prior to using it to drive the sensor. The phase control block points to a shift register position. Changing the register position read changes the output signal phase, and thus the overall loop phase. This strategy to adjust phase and close the loop, though, has a drawback. Given that oscillation frequency changes with temperature, so does the phase step between two consecutive shift register bits. As an example, consider that the MEMS resonates around $f_{res} = 146$ *kHz* at $35°C$ while having a temperature frequency coefficient of -200 $Hz/°C$. With a sampling frequency of $f_{sampl} = 5.55$ *MS/s* and three interpolators ($\times 8$ interpolation), a single period uses $8 f_{sampl}/f_{res} = 304$ consecutive bits of the register, having a phase resolution of $360°/304 = 1.184°/bit$. Now, if temperature decreases $10°C$, resonance frequency would increase 2 *kHz* and use 300 consecutive register bits. This means that phase resolution would be $1.200°/bit$. As a consequence, if the shift register bit read is kept unchanged, in this case of a 1024-bit shift register, in the worst case (this is, reading the 1024th bit), phase error can be up to 16.4°, that would be observed with an important reduction of the output signal. Possible solutions may be reducing the length of the shift register in order to allow space only for a single period. However, in order to allow measurements in all the temperature range of, for example, automotive applications ($-40°C$ - $125°C$), register may only be reduced to 512 bits, being the higher temperature (with the lowest resonance frequency of 128 *kHz*) the limit. On the other temperature limit, this is, when resonance frequency is maximum, the number of samples per period would be minimum and hence the phase step would be maximum. In this case, a small temperature variation will have an increased impact in phase. The phase error $|\phi_\epsilon|$ associated with a variation in temperature if the register bit reading remains unchanged can be expressed as

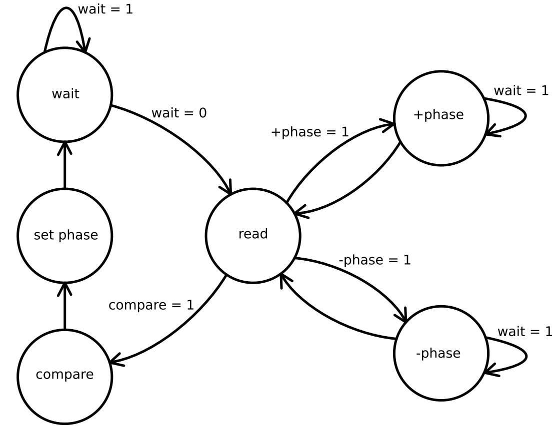

Fig. 6. Phase control state diagram.

$$|\phi_\epsilon| = \frac{360° N TC_f}{2^M f_S} |\Delta T| \quad (14)$$

where N is the read shift register position, TC_f is the resonance frequency temperature coefficient, f_S is the sampling frequency, M is the number of interpolators and ΔT is the temperature difference. For this reason, a periodic phase adjustment is necessary. This phase issue may not be found in systems implementing a PLL instead. However, in case of using a PLL other difficulties such as complexity, design time and power consumption would arise.

MEMS phase at resonance frequency is 0°, while at lower frequencies it approaches to 90° and at higher frequencies it goes to −90°. If the phase of the other loop blocks is also 0°, the entire loop, comprising the electronics and the MEMS, would be locked at that phase and the device would work at resonance. In this situation, output amplitude is maximum. If loop phase deviates from the ideal value of 0°, the device would work at a shifted phase and its amplitude would decrease. For this reason, the phase control block operates with the principle that when the correct phase is set, output signal is maximum. This block has two modes of operation: 1) Burst mode and 2) normal mode. In the burst mode, the phase is not locked (for example, during startup) and the phase adjustment is performed at high speed. In normal mode, the phase is already locked but it is checked anyway in case some thermal or mechanical variation has made the loop phase to change. In both cases, the same algorithm is run, depicted in Fig. 6. The states in the diagram are:

- wait: the system is measuring and phase adjustment is stopped.
- read: in this state, 8 samples of the filter output data are read, averaged and stored. In order to provide a trade-off between noise data and phase adjustment speed, the signal read by the algorithm is the 1 *kHz* LPF output signal. Doing so, after each data change settling time is much shorter than taking signal from the 10 *Hz* output filter.
- +phase: increments output phase and waits until filter output signal settles. The increment is made by increasing the shift register read address. In normal mode, steps are

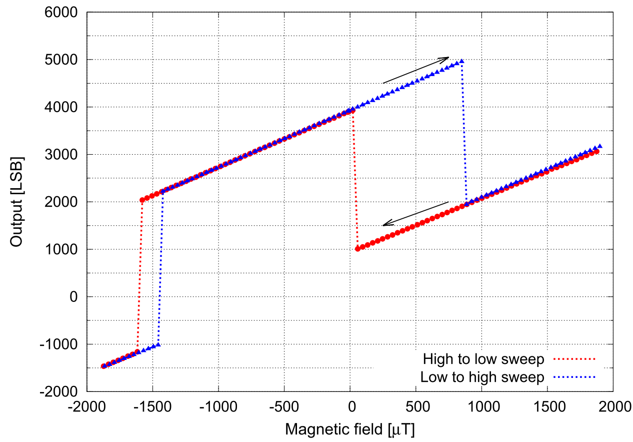

Fig. 7. Raw data output in LSB after digital processing but before offset compensation. Each value is the average of 8 measurements. It is possible to observe the offset added when electrostatic driving is enabled.

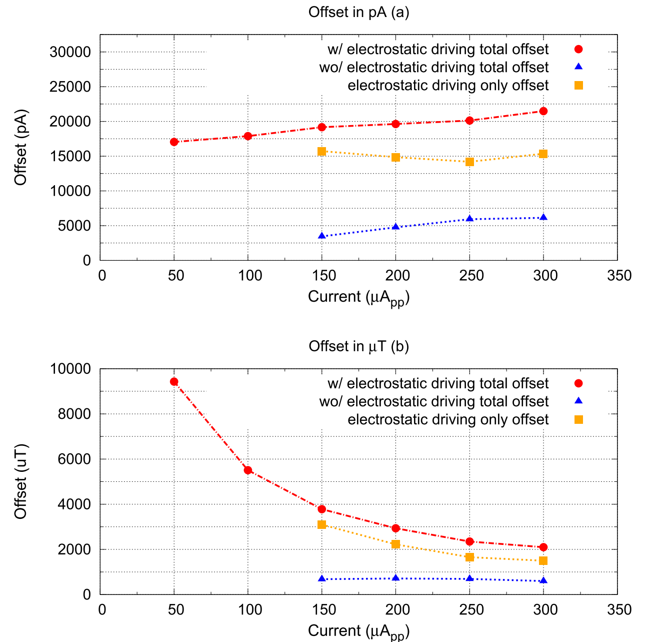

Fig. 8. Sensor offset as a function of current driving in *pA* (a) and *µT* (b). Offset with electrostatic driving enabled (red line) is much higher than when disabled (blue line). Electrostatic driving only offset is represented by the orange line.

unitary while in burst mode the increment is 8 register positions.

- −phase: same as the previous state but in the other direction.
- compare: this state compares the three stored samples and decides which phase provides the higher output.
- set phase: new phase is set.

In burst mode, phase is checked every 20 *ms* and no averaging is performed as a fast phase locking is preferred over accuracy. Here, the main time limiting factor is the filter settling time. In normal mode, phase adjustment is made every 30 *ms*, even though slower adjustment can be made.

A. Inversion and Amplitude Control

To the best of our knowledge, articles found in the literature with closed-loop sensing permanently drive the sensor with both current and electrostatic driving. While the first is indispensable to generate the Lorentz force and detect magnetic field, the second can be disabled if signal at the output of the bandpass filter is large enough to allow the zero-crossing detector to work properly. In this work, electrostatic driving is selectively enabled when signal is dangerously low to keep oscillation working, while it is disabled if output signal increases, resulting in an offset reduction and range increase. This electrostatic driving control has been implemented digitally with some hysteresis as shown in Fig. 7. Furthermore, it is depicted in Fig. 2c named as “Amplitude detect”.

VII. Experimental Results

In order to perform the measurements, the sensor was placed inside a custom Helmholtz coil. Sensor voltage biasing was set to 1 V and electrostatic driving rms amplitude, when enabled, was set to 6 mV_{rms}. Temperature has not been controlled during measurements, but few hours have been left between startup and measurements in order to allow temperature to settle.

A. Sensor Sensitivity and Offset

Sensor offset for the cases where electrostatic driving is enabled and disabled is shown in Fig. 8. Offset is shown in sensor output current units (pA) and in magnetic field units (μT). Showing the offset in both units helps to identify the offset source and behaviour as a function of driving current. In Fig. 8a offset with electrostatic driving enabled and disabled increases with the same slope, which suggests that this offset is a consequence of parasitic feedthrough between Wire and Sense nodes. This is demonstrated by the fact that, when offset due to current driving only is suppressed from the offset when electrostatic driving is enabled, it results in an approximately flat line representing the offset due to electrostatic driving only. Given that this driving is constant, so is the offset in current units. Analysing offset in magnetic field units in Fig. 8b shows that offset due to current feedthrough is 793 μT in all cases, being constant along current driving because both current feedthrough offset and sensitivity depend on current driving, a dependence that cancels out. Moreover, most offset is due to electrostatic driving. In the best case analysed, i.e. with 300 μA_{rms} and sensitivity $S = 9.75$ $pA/\mu T$, offset due to electrostatic driving is only 1324 μT.

B. Bias Instability and Noise

In order to analyse offset instability, Overlapping Allan deviation has been used due to the smoother curve it provides compared with Allan deviation [38]. The Overlapping Allan deviation obtained with the sensor data is shown in Fig. 9 with measurements made at a sampling frequency of 10 Hz. Offset instability has been obtained from the region where the Allan deviation is flat [39]. When electrostatic driving is enabled, offset instability is 125 nT, with an integration time of 23.4 s. On the other case, when electrostatic driving is not used, offset instability is 104 nT with an integration time of 15.5 s. As it

TABLE I
COMPARISON OF MAGNETOMETERS IN THE LITERATURE

Device	Offset (μT)	Current (μA_{rms})	Biasing (V)	FSR (mT)	Noise ($nT/\sqrt{Hz}$)	Nonlinearity %	Type
LIS3MDL [43]	±100	270^a	n/a	±1,6	$320^{b,c}$	±0.12	AMR
MAG3110 [42]	±100	137.5^a	n/a	±1,0	250^b	±0.3	MTJ
AK8963 [9]	±75	5000^a	n/a	±4,912	n/a	n/a	Hall sensor
BMC150 [40]	±40	4900^a	n/a	±2.5	300^b	1.0	Flip Core and Hall sensor
[17]	30^d	100	n/a	0.3	10	1.0	MEMS AM
[19]	n/a	300	1	±2,0	10	n/a	MEMS off-resonance
[15]	31 (25000^e)	900	4	±0.4	400	n/a	MEMS Current chopping
[20]	n/a	107	2	±2,4	380	2.0	MEMS multi-loop
[21]	2	100	6	±5.5	200	<0.2	MEMS multi-loop off-resonance
[27]	15 (310^e)	4600	8	±0.4	70	n/a	MEMS bias chopping
This work	1324 w/, 793 wo/	300	1	±1.0	550	±1.5	MEMS with digitally closed loop

[a] Current for highest resolution mode.
[b] Noise is in rms units.
[c] Noise for X/Y axis. For Z axis it is 410 μT_{rms}
[d] Extrapolated from article Fig. 13.
[e] Initial offset.

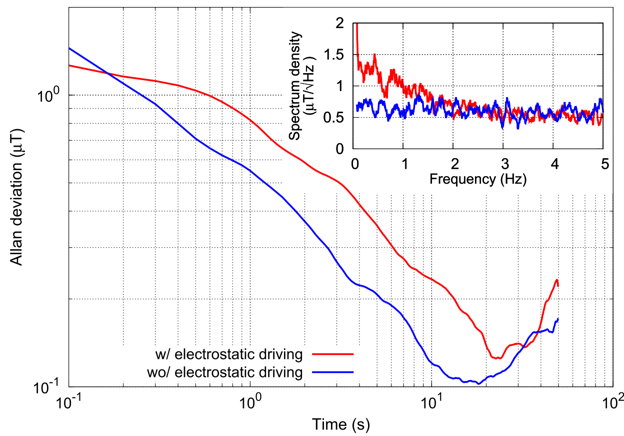

Fig. 9. Overlapping Allan deviation and noise spectral density (inset) of output signal with (red) and without (blue) electrostatic driving.

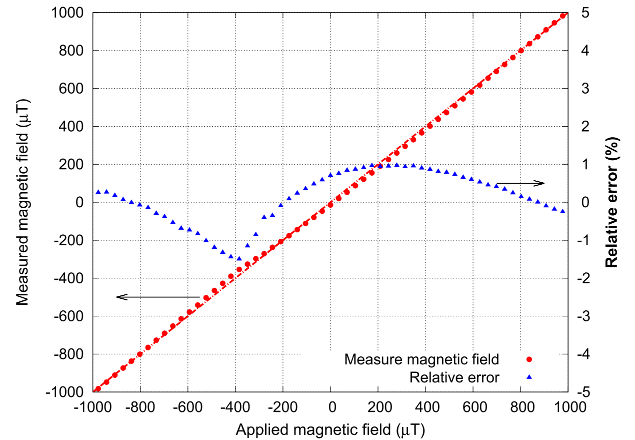

Fig. 10. Sensor measured magnetic field versus applied magnetic field (red) and relative error (blue) for a driving current of 300 μA_{rms}. Data shown is an average of 4 samples.

can be seen, in both cases bias instability is similar, and removing electrostatic driving does not worsen this figure.

Noise spectrum density has been used to analyse sensor noise, shown in Fig. 9 inset. In both cases noise spectrum is almost flat, although in the case when electrostatic driving is enabled, there is some low frequency noise increase. This is thought to be caused by a slow temperature drift during the measurement. In both cases, dominant white noise is 550 $nT/\sqrt{Hz}$, which is larger than the estimated noise in section V. It must be taken into account, though, that various approximations are done during the noise estimation which may be the cause of this 2-3 times mismatch. This is reasonable given that some parasitic capacitances can not be measured, either at the device packaging level and at the chip-PCB interface.

C. Sweep and Measurement Error

Finally, a magnetic field sweep between ±1 mT with 35 μT steps has been performed in order characterize the sensor. The result is shown in Fig. 10. Along the measured range, there is a transition around -400 μT between measurements made with the electrostatic driving enabled and disabled. As it can be seen, the nonlinearity at this point is -1.5%. Some nonlinearity is observed when electrostatic driving is disabled. Its main source is thought to be a combination of ADC gain error and MEMS nonlinearity.

In principle, MEMS measuring range is unlimited if current driving is conveniently reduced. A wider magnetic field sweep has been performed with a driving current of 25 μA_{rms} with a maximum measurement range of ±13 mT, being the Helmoltz coil maximum magnetic field the limiting factor, not the sensor.

VIII. COMPARISON WITH PREVIOUS WORKS

In table I the most relevant figures to evaluate state-of-the-art magnetometers have been included from both commercial devices and academic MEMS magnetometers. In order to allow comparison, only MEMS magnetometers with AM output have been included.

Offset is one of the main concerns in any sensor output. For this reason, commercial devices offer offset removal capabilities [40]–[42], but its offset tends to be large

and unpredictable. Some works [15], [27] propose strategies to reduce offset and improve biasing instability. Such strategies, though, require the use of electrostatic driving, which is an important source of offset itself. Our work presents an analysis of the driving offsets. This knowledge will be very useful during the integration of the MEMS and the electronics in the same die area. Similarly, some works [19]–[21] do not quantify offset, and when they do, it is very low. This is a consequence of not using electrostatic driving, which is the same approach proposed in our work. However, these works use bulky lock-in amplifiers or other instruments to drive the sensor in closed loop, or drive it in open-loop. Hence, our work explores the benefits and disadvantages of using different driving strategies while, at the same time, proposing a resonator loop.

In terms of noise, the best figures in the literature are those in [17] and [19]. In both cases, an accurate design of the device results in excellent sensitivities and the lowest noise figures to the best of our knowledge. However, commercial instruments were used to close the loop and perform the measurements, meaning that there is still work to be done until the total integration of the system. Our work shows noise higher than most works, but using relatively low current driving and DC voltage across the MEMS device. This is important because most works use high biasing voltages from 4 V up to 8 V [15], [21], [27]. While this is a way to increase device sensitivity and SNR without increasing power consumption, maximum voltages that the technology can safely withstand must be taken into account. Hence, biasing voltage should be compatible with 3.3 V and even 1.5 V supplies.

As briefly presented above, most works make use of lock-in amplifiers to close the loop and only a few close the loop either on-chip or using electronics on a PCB [11], [12], [23]. Moreover, no previous works have been found where the loop control and data processing are performed digitally, which is one of the key advantages presented in this work and the first step for the introduction of MEMS magnetometers into the market.

IX. Conclusion

In this work a Lorentz force based resonant MEMS magnetometer has been presented. A mixed-signal processing chain has been proposed to keep the MEMS device in a self-sustained oscillation loop at its resonance frequency.

Doing so, loop phase locking is achieved and correct locking can be periodically controlled. Moreover, a strategy to reduce sensor offset has been proposed which allows the system to keep oscillation when the measured magnetic field is low by selectively enabling and disabling electrostatic driving.

The proposed digital system has been coded in VHDL and implemented in an FPGA as a proof of concept prior to its integration in a System-on-Chip. A 550 $nT/\sqrt{Hz}$ total output noise has been obtained with an offset of 793 μT when electrostatic driving is disabled, which represents a 40.1% reduction. However, a better offset figure is expected to be achieved in an integrated implementation.

References

[1] *Technology Trends for Inertial MEMS*, Yole Développement, Villeurbanne, France, 2012.

[2] *3-Axis Consumer Gyroscopes*, Yole Développement, Villeurbanne, France, Nov. 2012.

[3] B. Eyre, K. S. J. Pister, and W. Kaiser, "Resonant mechanical magnetic sensor in standard CMOS," *IEEE Electron Device Lett.*, vol. 19, no. 12, pp. 496–498, Dec. 1998.

[4] S. Kádár, A. Bossche, P. M. Sarro, and J. R. Mollinger, "Magnetic-field measurements using an integrated resonant magnetic-field sensor," *Sens. Actuators A, Phys.*, vol. 70, no. 3, pp. 225–232, Oct. 1998.

[5] *AKM8975/AK8975C 3-Axis Electronic Compass*, Asahi Kasei Microdevices Corp., Tokyo, Japan, 2010.

[6] *HMC1043 3-Axis Magnetic Sensor*, Honeywell, Charlotte, NC, USA, Nov. 2010.

[7] *TMR Angle Sensor With Digital Output*, TDK, Chiyoda, Japan, Dec. 2017.

[8] *Magnetic Sensor Market and Technology Report*, Yole Développement, Villeurbanne, France, Aug. 2017.

[9] *AK8963 3-Axis Electronic Compass Datasheet*, Asahi Kasei, Chiyoda, Japan, 2010.

[10] J. Lenz and A. S. Edelstein, "Magnetic sensors and their applications," *IEEE Sensors J.*, vol. 6, no. 3, pp. 631–649, Jun. 2006.

[11] R. Sunier, T. Vancura, Y. Li, K. U. Kirstein, H. Baltes, and O. Brand, "Resonant magnetic field sensor with frequency output," *J. Microelectromech. Syst.*, vol. 15, no. 5, pp. 1098–1107, Oct. 2006.

[12] B. Bahreyni and C. Shafai, "A resonant micromachined magnetic field sensor," *IEEE Sensors J.*, vol. 7, no. 9, pp. 1326–1334, Sep. 2007.

[13] V. T. Rouf, M. Li, and D. A. Horsley, "Area-efficient three axis MEMS Lorentz force magnetometer," *IEEE Sensors J.*, vol. 13, no. 11, pp. 4474–4481, Nov. 2013.

[14] V. Kumar, M. Sebdani, and S. Pourkamali, "Sensitivity enhancement of a Lorentz force MEMS magnetometer with frequency modulated output," *J. Microelectromech. Syst.*, vol. 26, no. 4, pp. 870–878, Aug. 2017.

[15] M. Li and D. A. Horsley, "Offset suppression in a micromachined Lorentz force magnetic sensor by current chopping," *J. Microelectromech. Syst.*, vol. 23, no. 6, pp. 1477–1484, Dec. 2014.

[16] H. Emmerich and M. Schofthaler, "Magnetic field measurements with a novel surface micromachined magnetic-field sensor," *IEEE Trans. Electron Devices*, vol. 47, no. 5, pp. 972–977, May 2000.

[17] J. Kyynäräinen, "A 3D micromechanical compass," *Sens. Actuators A, Phys.*, vol. 142, no. 2, pp. 561–568, Apr. 2008.

[18] M. Li, V. T. Rouf, M. J. Thompson, and D. A. Horsley, "Three-axis Lorentz-force magnetic sensor for electronic compass applications," *J. Microelectromech. Syst.*, vol. 21, no. 4, pp. 1002–1010, Aug. 2012.

[19] G. Langfelder and A. Tocchio, "Operation of Lorentz-force MEMS magnetometers with a frequency offset between driving current and mechanical resonance," *IEEE Trans. Magn.*, vol. 50, no. 1, pp. 1–6, Jan. 2014.

[20] P. Minotti, S. Brenna, G. Laghi, A. G. Bonfanti, G. Langfelder, and A. L. Lacaita, "A sub-400-nT/$\sqrt{}$Hz, 775-μW, multi-loop MEMS magnetometer with integrated readout electronics," *J. Microelectromech. Syst.*, vol. 24, no. 6, pp. 1938–1950, Dec. 2015.

[21] G. Laghi, C. R. Marra, P. Minotti, A. Tocchio, and G. Langfeld, "A 3-D micromechanical multi-loop magnetometer driven off-resonance by an on-chip resonator," *IEEE J. Microelectromech. Syst.*, vol. 25, no. 4, pp. 637–651, Aug. 2016.

[22] W. Zhang and J. E.-Y. Lee, "Frequency-based magnetic field sensing using Lorentz force axial strain modulation in a double-ended tuning fork," *Sens. Actuators A, Phys.*, vol. 211, pp. 145–152, May 2014.

[23] M. Li, S. Sonmezoglu, and D. Horsley, "Extended bandwidth Lorentz force magnetometer based on quadrature frequency modulation," *J. Microelectromech. Syst.*, vol. 24, no. 2, pp. 333–342, 2015.

[24] P. Michalik, D. Fernández, M. Wietstruck, M. Kaynak, and J. Madrenas, "Experiments on MEMS integration in 0.25 μm CMOS process," *Sensors*, vol. 18, no. 7, p. 2111, Jun. 2018.

[25] P. Michalik, J. M. Sánchez-Chiva, D. Fernández, and J. Madrenas "CMOS BEOL-embedded lateral accelerometer," in *Proc. IEEE Sensors*, Nov. 2015, pp. 1–4.

[26] F. Y. Kuo, C. Y. Lin, P. C. Chuang, C. L. Chien, Y. L. Yeh, and S. K. A. Wen, "Monolithic multi-sensor design with resonator-based MEMS structures," *IEEE J. Electron Devices Soc.*, vol. 5, no. 3, pp. 214–218, May 2017.

[27] S. Sonmezoglu and D. A. Horsley, "Reducing offset and bias instability in Lorentz force magnetic sensors through bias chopping," *J. Microelectromech. Syst.*, vol. 26, no. 1, pp. 169–178, Feb. 2017.

[28] J. Valle, D. Fernández, J. Madrenas, and L. Barrachina, "Curvature of BEOL cantilevers in CMOS-MEMS processes," *J. Microelectromech. Syst.*, vol. 26, no. 4, pp. 895–909, Aug. 2017.

[29] J. Valle, D. Fernández, and J. Madrenas, "Experimental analysis of vapor HF etch rate and its wafer level uniformity on a CMOS-MEMS process," *J. Microelectromech. Syst.*, vol. 25, no. 2, pp. 401–412, Apr. 2016.

[30] A. Witvrouw *et al.*, "Comparison between wet HF etching and vapor HF etching for sacrificial oxide removal," *Micromach. Microfabrication Process Technol.*, vol. 25, pp. 130–142, Aug. 2000.

[31] C. H. Tsau and T. K. Nunan, "Silicon-rich nitride etch stop layer for vapor HF etching in MEMS device fabrication," U.S. Patent 0 320 548 A1, Dec. 23, 2010.

[32] *Arduino Due Product Page*. Accessed: Oct. 2018. [Online]. Available: https://store.arduino.cc/arduino-due

[33] *AN-1515 A Comprehensive Study of the Howland Current Pump*, Texas Instrum., Dallas, TX, USA, Apr. 2013.

[34] T. B. Gabrielson, "Mechanical-thermal noise in micromachined acoustic and vibration sensors," *IEEE Trans. Electron Devices*, vol. 40, no. 5, pp. 903–909, May 1993.

[35] *THS4121 Fully Differential Amplifier Datasheet*, Texas Instrum., Dallas, TX, USA, Oct. 2004.

[36] I. Mateos, "Design and assessment of a low-frequency magnetic measurement system for eLISA," Ph.D. dissertation, Institut d'Estudis Espacials Catalunya, Institut de Ciències de l'Espai, Barcelona, Spain, 2015. [Online]. Available: http://www.ice.csic.es/files/mateos/thesisNacho.pdf

[37] D. A. Johns and K. Martin, *Analog Integrated. Circuit Design*. New York, NY, USA: Wiley, 1997, p. 450.

[38] R. Song, X. Chen, and H. Huang, "Nonstationary dynamic stochastic error analysis of fiber optic gyroscope based on optimized Allan variance," *Sens. Actuators A, Phys.*, vol. 276, pp. 26–33, Jun. 2018.

[39] N. El-Sheimy, H. Hou, and X. Niu, "Analysis and modeling of inertial sensors using Allan variance," *IEEE Trans. Instrum. Meas.*, vol. 57, no. 1, pp. 140–149, Jan. 2008.

[40] *BMC150 6-Axis eCompass*, Bosch, Reutlingen, Germany, Jul. 2014.

[41] *AN4602 Application Note. LIS3MSL: Three-Axis Digital Output Magnetometer*, STMicroelectron., Geneva, Switzerland, Dec. 2014.

[42] *Xtrinsic MAG3110 Three-Axis, Digital Magnetometer*, NXP, Eindhoven, The Netherlands, Feb. 2013.

[43] *LIS3MDL Digital Output Magnetic Sensor: Ultra-Low-Power, High-Performance 3-Axis Magnetometer Datasheet*, STMicroelectron., Geneva, Switzerland, Dec. 2014.

Josep Maria Sánchez-Chiva was born in Barcelona, Spain, in 1989. He received the B.Sc. in telecommunication engineering and the M.Sc. degree in electronic engineering from the Universitat Politècnica de Catalunya (UPC), in 2011 and 2014, respectively, where he is currently pursuing the Ph.D. degree with the Electronic Engineering Department. From 2012 to 2013, he made an internship as an Analog Designer with Broadcom, and in 2016 as a Test Engineer with Indra Testing Satellite Communications PCBs for the European Space Agency. His research interests include MEMS sensors readout circuits, integrated analog low power design, and energy harvesting.

Juan Valle was born in Lugo, Spain, in 1977. He received the M.Sc. degree in physics and the M.Sc. degree in industrial engineering from Universidad Alfonso X El Sabio (UAX), Madrid, Spain, in 2000 and 2002, respectively, and the International master's degree in theoretical and practical application of finite element method and CAE simulation from the Universidad Nacional a Distancia (UNED), Madrid, Spain, in 2004. He is currently pursuing the Ph.D. degree in electronic engineering with the Universitat Politècnica de Catalunya (UPC), Barcelona, Spain.

From 2001 to 2002, he was a Microsystems (MEMS) and Nanotechnology Consultant for the National Institute for Aerospace Technology (INTA). He specialized on multiphysics simulations before joining Delphi Diesel Systems in 2004 as an Analyst Engineer, and joined Baolab Microsystems in 2005, where he researched on the fields of MEMS sensors and micromanufacturing processes for nine years, and also filled ten patent applications on related fields. He devised design techniques applicable for the MEMS fabrication inside the CMOS BEOL. Using these techniques, he is developing the first CMOS-MEMS 3 axis magnetometer aimed at mass production.

Daniel Fernández was born in Barcelona, Spain, in 1979. He received the M.Sc. degree in telecommunications engineering, the Ph.D. *(cum laude)* and M.B.A. degrees from the Universitat Politècnica de Catalunya (UPC), Barcelona, Spain, in 2004, 2008, and 2009, respectively.

From 2008 to 2010, he was a Post-Doctoral Researcher with the Electronic Engineering Department, UPC, in CMOS surface micromachining, circuits and control architectures for MEMS sensors and actuators, translinear circuits for analog signal processing, and digital implementations of power converters. From 2010 to 2014, he was a Principal ASIC Engineer with Baolab Microsystems, developing circuits and architectures for CMOS MEMS/NEMS-based products, and as an ASIC Design Engineer Contractor for the European Space Agency, designing radiation-hardened integrated-circuits and interface blocks for space exploration in interplanetary missions. He is currently a Chief Technology and Science Officer with Nanusens, Cerdanyola del Vallès, Spain, where he works towards the development of innovative technologies and products based on MEMS.

Jordi Madrenas received the degree in telecommunication engineering in 1986 and the Ph.D. degree in 1991.

He coordinates the Integrated Smart Sensors and Health Technologies (ISSET) Research Group, UPC. From 2000 to 2003, he was the Vice Dean of Studies with the Telecommunication Engineering School of Barcelona, UPC. He is currently an Associate Professor with the Department of Electronic Engineering, Universitat Politècnica de Catalunya (UPC), Barcelona, Catalunya, Spain. He has participated in five European projects and has coordinated six Spanish national research projects and several contracts with companies. He currently leads a national project on microelectromechanical systems (MEMS) on-chip and microsensor bioinspired signal processing. He has coauthored 35 scientific journals, more than 130 international conference papers, two books, five book chapters, and holds one international patent. His current research interests include analog, mixed-signal and digital VLSI and FPGA design, CMOS-MEMS design and conditioning, ultra-low-power design, bioinspired/neuromorphic system implementation, and rad-hard mixed-signal circuits.